Prabha Materials Science Letters
Vol. 5, No. 1, 159-173, 2026
https://doi.org/10.33889/PMSL.2026.5.1.008

Growth Behavior of Nano-Hydroxyapatite as Affected by Synthesis Temperature and Ca/P Ratio of Precursors

Mayora Varshney
School of Applied and Life Sciences,
University Institute of Technology, Uttaranchal University, Dehradun, 248007, Uttarakhand, India.
E-mail: mayoravarshney@uumail.in

Aditya Sharma
Department of Physics,
University of Petroleum and Energy Studies, Dehradun, 248007, Uttarakhand, India.
Corresponding author: adityaiuac@gmail.com

B. H. Lee
Advanced Analysis Centre,
Korea Institute of Science and Technology, Seoul, 02792, South Korea.
E-mail: bhlee@kist.re.kr

Sung Ok Won
Advanced Analysis Centre,
Korea Institute of Science and Technology, Seoul, 02792, South Korea.
E-mail: sowon@kist.re.kr

(Received on December 21, 2025; Revised on February 3, 2026; Accepted on February 7, 2026)

Abstract
The synthesis of bio-relevant calcium phosphates has attracted considerable attention, as even minor deviations in the stoichiometric Ca/P ratio ($1.5 \leq Ca/P \leq 1.67$) can induce the formation of multiple crystalline phases. In this study, the combined influence of nominal Ca/P ratio and synthesis temperature on the phase evolution of calcium phosphates was systematically investigated. Calcium phosphate powders with Ca/P ratios of 1.4, 1.5, 1.6, and 1.67 were synthesized over a wide temperature range, from ice-bath conditions to 200°C, followed by calcination at 800°C, while maintaining a constant pH of 10 for all samples. Regardless of the synthesis temperature and Ca/P ratio, calcium-deficient hydroxyapatite (CDHA) was initially precipitated. For nominal Ca/P ratios of 1.4 and 1.5, CDHA synthesized under ice-bath conditions transformed into β-tricalcium phosphate (β-TCP) after calcination. Samples with Ca/P = 1.6 exhibited mixed phases of hydroxyapatite (HA) and β/α-TCP upon calcination, independent of synthesis temperature. In contrast, HA was obtained after calcination of CDHA samples synthesized at temperatures ≥50°C with a Ca/P ratio of 1.67. The observed phase diversity is rationalized in terms of temperature-dependent Ca^{2+} ion migration at the molecular level, governing compositional homogeneity and phase stability.

Keywords- Ca/P ratio, Calcium-deficient hydroxyapatite (CDHA), β-TCP, Ice bath.

1. Introduction

The manufacturing of calcium orthophosphates has garnered significant scientific interest due to their resemblance to biologically calcified tissues in mammals and their remarkable biocompatibility (Pillai and Sglavo, 2015; Li et al., 2018; Glazov et al., 2022; Das et al., 2023; Mandic et al., 2023). In last decades, calcium phosphate ceramics have been applied in orthopedics and dentistry applications by considering excellent stability, osteoinductivity, bioactivity, etc., (Pillai and Sglavo, 2015; Li et al., 2018; Glazov et al., 2022; Das et al., 2023; Mandic et al., 2023). There are attempts to design artificial bone crafts from the laboratory-grown calcium phosphates (Daculsi, 1998; Lima et al., 2020; Glazov et al.,

2022; Varshney et al., 2025). However, there are issues related to the preparation and bioactivity of a certain phase of calcium phosphate over the other phases (Kannan et al., 2005; Abdel-Fattah et al., 2008; Chen et al.; 2024; Elgharbawy et al., 2024; Humbert et al., 2024; Mutlu et al., 2024; Viragova et al., 2024).

It has been known that the laboratory-grown calcium phosphates ceramics are composed of more than one phase (Daculsi et al., 1998; Pillai and Sglavo, 2015; Li et al., 2018, Lima et al., 2020; Glazov et al., 2022; Das et al., 2023; Mandic et al., 2023; Varshney et al., 2025). The constituent phases are intimately mixed at the submicron level and strongly integrated and, therefore, cannot be separated from each other. This is because a little deviation in the nominal Ca/P ratio and/or other synthesis parameters can assimilate diverse chemical kinematics among the starting reagents of calcium and phosphorus and, therefore, lead to the formation of diverse phases of calcium phosphate (Kannan et al., 2005; Abdel-Fattah et al., 2008; Chen et al.; 2024; Elgharbawy et al., 2024; Humbert et al., 2024; Mutlu et al., 2024; Viragova et al., 2024). Several attempts have been made to synthesis the single-phase calcium-deficient hydroxyapatite (CDHA), tri-calcium phosphate (β/α-TCP), and hydroxyapatite (HA) by applying the capping agents (like Ethylenediaminetetraacetic acid (EDTA), Polyethylene Glycol (PEG), etc.), microwave irradiation, using the autoclaves, and supplying additional CO_3^{-2} or SO_4^{-2} ions for controlling the initial precipitation and phase formation (He et al., 2016; Samanta et al., 2019; Hu et al., 2022; Yang et al., 2023; Bristy et al., 2025). The Ca and P deficiencies and the kinematics among them are the major factors that control the final phase of calcium phosphates (Dorozhkin, 2012; Blum et al., 2021). The reaction temperature, which regulates the Gibbs free energy of the constituent nuclei of the calcium phosphate precipitates, is known to be the key factor for the stabilization/growth of a certain phase during the precipitation (Carino et al., 2018; Luo et al., 2025). It was speculated that an increase in reaction temperature can increase the Gibbs free energy and, consequently, a greater driving force for precipitation. In other reports, it was also reported that the Ca deficiencies would favor the TCP phase formation; however, the lower Ca deficiencies lead to HA phase stabilization from the chemically prepared CDHA (Li et al., 2018; Hu et al., 2022; Mandic et al., 2023). It was also assumed that the Ca deficiency leads to incorporation of HPO_4^{2-} ions in the lattice, which, indeed, promotes TCP phase formation (Mandic et al., 2023; Raudonyte-Svirbutaviciene et al., 2023). Besides the temperature, the pH value of precursors has also been reported to affect the precipitate formation (Dorozhkin, 2012; Carino et al., 2018; Vilela et al., 2021). The lower pH (4-6) value of precursors required a higher temperature for the precipitation; however, the higher pH (10-12) grown samples were densely precipitated even at a lower temperature (Dorozhkin, 2012; Vilela et al., 2021).

The present study is an attempt to synthesize the single-phase calcium phosphates by adjusting the temperature and Ca/P ratio of the precursors with the reaction condition of constant pH ~10. The precipitates of CDHA were subjected to calcination at 800°C, which resulted in the formation of controlled β-TCP+ HA bi-phasic ceramics, depending on the nominal Ca/P ratios and precursor temperature. Along with this, single-phase β-TCP has been achieved at two different Ca/P ratios (i.e., Ca/P = 1.4 and 1.5) while the *ice-bath* prepared CDHA was subjected to calcination at 800°C. Simultaneously, single-phase HA was also achieved at Ca/P ratio of 1.67, while the CDHA (which was prepared at and above the 100°C precursor temperature) was calcined at 800°C. The as-synthesized and calcined powders were characterized by X-ray diffraction (XRD), Raman spectroscopy, and transmission electron microscopy (TEM) to identify the phase composition/crystallinity and size/shape of calcium phosphates.

2. Experimental Details

2.1 Preparation of Samples

The analytical grade calcium nitrate tetrahydrate ($Ca(NO_3)_2.4H_2O$) and ammonium phosphate, $(NH_4)_2HPO_4$, were used as the starting materials without further purification. For the preparation of different calcium phosphate ceramics, predetermined Ca/P molar ratios of the suspensions (Ca/P = 1.4, 1.5, 1.6, and 1.67) were set by the slow addition (dropwise; ~5 mL/min) of ammonium phosphate solution to the continuously stirred (800 rpm) solution of calcium nitrate tetrahydrate. For the low-temperature synthesis of calcium phosphates, the solution beaker was kept in the *ice-tub* with magnetic stirring. Similarly, to prepare the calcium phosphates at a certain temperature, the hot plate was maintained at that desired temperature with magnetic stirring. In the present experiments, room temperature, 50°C, 100°C, 150°C, and 200°C were applied during the synthesis of different samples. The temperatures given are of the hot plate temperatures and do not represent the solution temperature inside of the beaker. A borosilicate glass beaker was used for synthesis and covered by aluminum foil. However, the beak portion of the beaker was made open to release the water vapors formed during the synthesis. The pH of the mixed solution was maintained at 10.0±0.2 by adding the NH_4OH solution. After stabilizing the pH, the solution was further stirred for 2 hr at the desired temperature. After the temperature treatment, the precipitates aged 24 hr. The aged samples were dried in the oven at 80°C overnight and then crushed by a mortar pestle until a fine powder could be achieved. The above-prepared samples (i.e., samples prepared at various synthesizing temperatures: *ice-bath*, room temperature, 50°C, 100°C, 150°C, and 200°C) were further subjected to high-temperature calcination to study the thermal stability of the products. Calcination of such as-synthesized powders was done at 800°C for 4 hr in air. The heating and cooling rates of the samples were 10°C/min. **Figure 1** shows the schematic of the synthesis procedure.

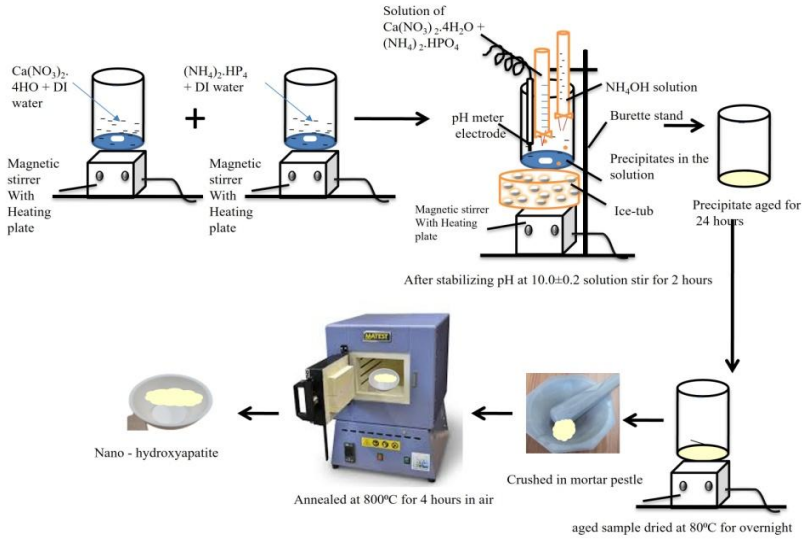

Figure 1. Schematic of synthesis procedure.

2.2 Characterization of Samples

XRD patterns of the samples were collected from the Bruker D8 Advance diffractometer with Cu Kα radiation (λ = 1.5418 Å), operated at 40 kV and 40 mA. The scan speed of the diffractometer was set to 1°/min with a step of 0.02°. The Raman spectra were collected by using the Renishaw (In-Via Raman) microscope with a Nd: YAG (neodymium-doped yttrium aluminum garnet) laser, which produces a

photon beam of the wavelength of 532 nm. Transmission electron microscopy measurements were performed by applying the Talos-F200X scanning-transmission electron microscope with an operational voltage capacity of 80- 200 kV. This TEM machine has the capabilities of element mapping from the samples using energy dispersive X-ray spectroscopy (EDS) measurements. The EDS has uncertainty, in analyzing the elemental concentrations, ranging from ±0.1–1wt %.

3. Results and Discussion

3.1 Phase Identification by XRD

XRD patterns of as-prepared samples (dried at 80°C), prepared with different Ca/P ratios and synthesis temperatures, are presented in **Figure 2**.

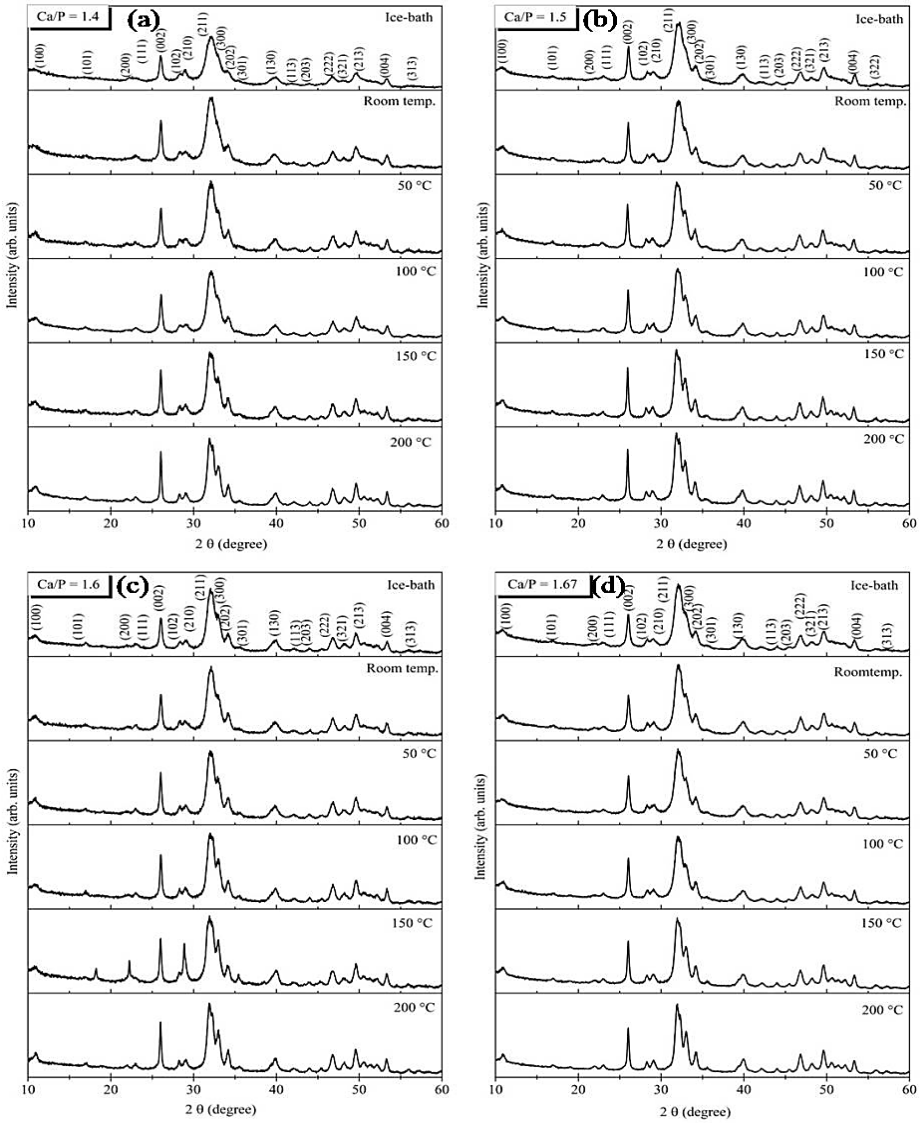

Figure 2. XRD patterns of different synthesis temperature grown samples, and Ca/P ratio of, (a) = 1.4, (b) 1.5, (c) 1.6, (d) 1.67. The XRD patterns of β-TCP phase and HA phase are indexed with standard JCPDF#04-001-7220 and JCPDF#04-007-2837 files, respectively.

Regardless of the changes in the nominal Ca/P ratios and synthesis temperature, all the diffraction peaks from each sample are identified and fairly matched with the hexagonal phase of CDHA (JCPDS#04-012-1115). This indicates the stability of the hexagonal CDHA phase under the present synthesis method. The diffraction peaks are broadened in the case of *ice-bath* and room temperature grown samples; however, they become intensified, narrower, and well resolved for the higher temperature synthesized samples (especially for the 200°C sample). This indicates *ice-bath*-grown (and 50°C-grown) samples are of poor crystallinity or composed of smaller-sized crystallites. A larger-sized particle with superior crystallinity is expected in the higher temperature prepared samples, which results in intense diffraction peaks. Average particle size is calculated (by selecting at least 06 intense XRD peaks) using the Scherrer relation: $D = 0.9\lambda/\beta Cos\theta$ (D is the particle size, λ is the wavelength of the used X-rays, and β is the full width at half maximum of the diffraction peaks). The calculated particle sizes are tabulated in **Table 1**. It is noticeable that the particle size is increasing with increasing synthesis temperature. Increase in the particle size with increase in the synthesis temperature is due to the thermal energy-induced precipitation rate and growth of crystallites (Vilela et al., 2021; Raudonyte-Svirbutaviciene et al., 2023).

Table 1. Average crystallite size, calculated from the XRD patterns, for different samples.

Ca/P ratio→	1.4	1.5	1.6	1.67
sample name↓	Size (nm) within error range of ± (0.5 nm to 1.3 nm)			
Ice-bath	22.1	24.2	23.1	22.7
Room temp.	25.0	27.1	26.0	24.5
50 °C	25.8	31.1	30.5	26.4
100 °C	26.6	30.7	34.2	30.1
150 °C	35.0	39.5	33.9	35.9
200 °C	40.9	42.1	41.7	38.9

3.2 Thermal Stability of the Samples

Figure 3(a-d) shows the XRD results from all of the samples, which were subjected to calcination at 800°C. It is certainly visible that the samples containing Ca/P = 1.4 and 1.5 ratios and grown at *ice-bath* conditions are composed of β-TCP phase (JCPDF#04-001-7220). Interesting variations in the phase composition were observed when the samples were subjected to the different synthesis temperatures (i.e., room temperature to 200°C). The growth of the HA phase (JCPDF#04-007-2837) with increasing the XRD peak intensity as a function of synthesis temperature is also apparent in the **Figure 3(a-d)**. In the present study, the growth of β-TCP phase for both Ca/P ratios (i.e., 1.4 and 1.5) under the condition of *ice-bath* is interesting. In previous reports, calcination of CDHA at 700°C - 1100°C temperatures have been reported to promote the growth of β-TCP phase while the Ca/P ratios were within the range of 1.4 - 1.5 (Pillai et al., 2015; Mandic et al., 2023). For example, Brazete et al. (2018) reported the β-TCP phase formation while the precursors of [Ca $(NO_3)_2.4H_2O$] and [$(NH_4)_2.4H_2O$] were mixed at room temperature with a Ca/P ratio of 1.5 and 1.51. They synthesized the β-TCP phase at Ca/P = 1.5 and the α-TCP phase at Ca/P = 1.51. Similarly, Hossain et al. (2023) have reported the formation of β-TCP phase by the precipitation of $Ca(CO_3)_2.4H_2O$ and (H_3PO_4) reagents at the Ca/P ratio of 1.5 and sintered at 900°C. In the present study, the growth of pure β-TCP phase at Ca/P = 1.4 is similar to the results of Kannan et al. (2005) and Abdel-Fattah et al. (2018).

In the present study, attention has been paid to understand the effect of synthesis temperature and Ca/P ratio of precursors for the growth of β-TCP or HA phases. Our experimental results convey that the Ca/P ratio is not only the factor that controls the growth of β-TCP or HA phases, but the synthesis temperature also helps in phase stability. All the samples grown at different Ca/P ratios and different synthesis temperatures obey CDHA phase. It is noticeable that the β-TCP phase is stable in the *ice-bath* and room

temperature-grown samples, while the Ca/P ratio was only 1.4 and calcination temperature was 800°C. In contrast to this, the sample grown at room temperature with Ca/P = 1.5 reflects the minor HA phase after calcination at 800°C. The 50°C, 100°C, 150°C, and 200°C synthesis temperatures were also applied to prepare the samples. After the calcination of such samples at 800°C, the XRD results show that the diffraction peaks from the HA phase have a significant contribution in the XRD data along with the β-TCP peaks (see **Figure 3(a-b)**. The HA peaks and their intensities are enhanced by increasing the synthesis temperature and indicate synthesis temperature dependency on the HA phase formation, even at the Ca/P = 1.4 and 1.5.

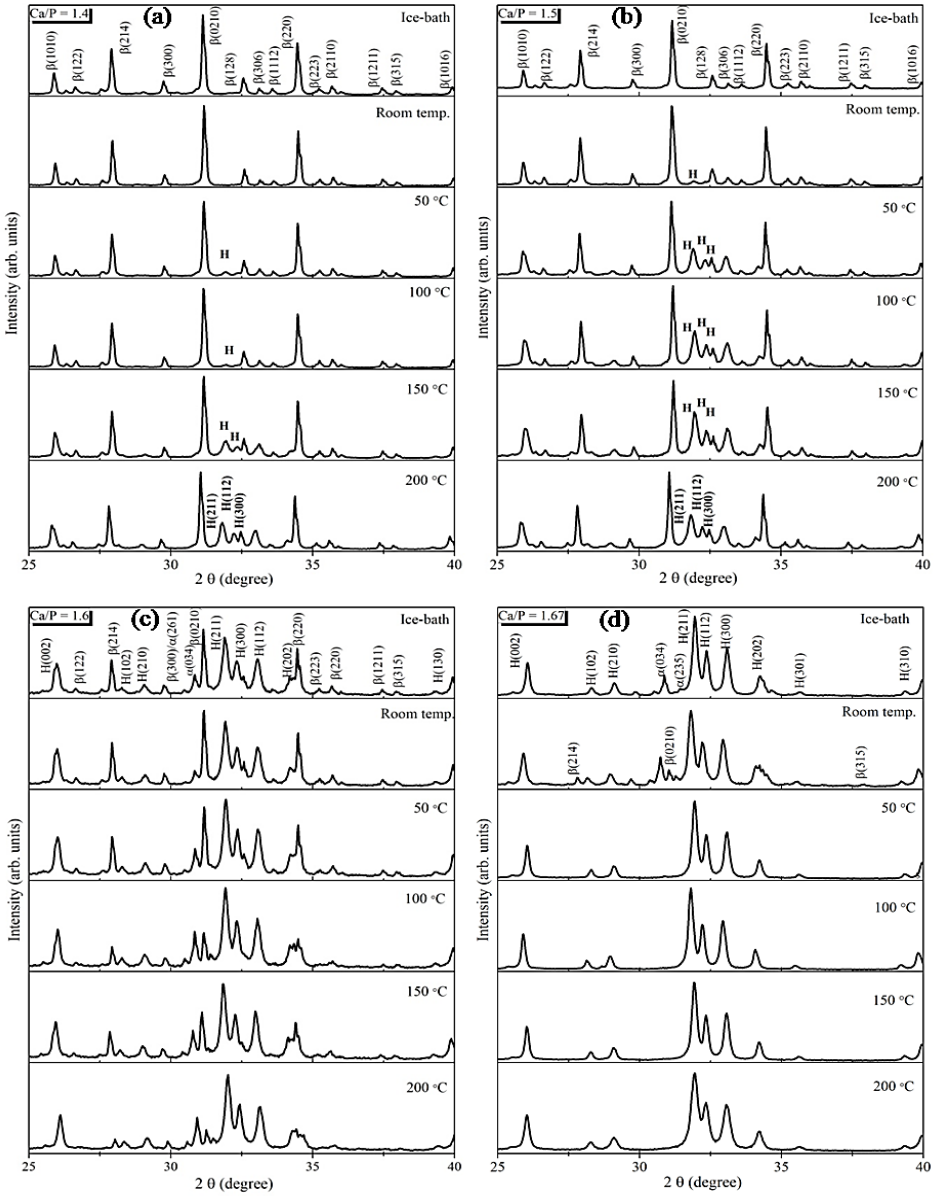

Figure 3. XRD patterns of different synthesis temperature grown samples, calcined at 800 °C and with Ca/P ratio of, (a) = 1.4, (b) 1.5, (c) 1.6, (d) 1.67. The symbols H, β, and α represent the HA, β-TCP and α-TCP phases, respectively.

It is noticed from **Figure 3(c)** that the contribution of XRD peaks from the HA phase is quite higher than the XRD peaks of the β-TCP phase. Furthermore, the XRD peaks of the β-TCP phase are weakened or even dissolved in those samples that were grown at higher synthesis temperatures. It is interesting to note that the Ca/P = 1.6 and 1.67 grown samples have shown some of the peaks from α-TCP phase along with β-TCP and HA phases. Though the XRD peak positions of α-TCP and β-TCP nearly overlap. Therefore, assignment of α-TCP phase is intriguing in the literature (Bajpai et al., 2017; Zhang et al., 2022; Glazov et al., 2022). The α-TCP phase is the sister phase of β-TCP and known as the metastable phase and has been reported as high temperature polymorphous (i.e., formed after annealing of β-TCP over 1100°C (Brazete et al., 2018; Glazov et al., 2022). Therefore, the existence of this phase is related to the diverse bonding between the Ca and P ions and may result from the calcination of the amorphous part of calcium phosphate, which co-exists with CDHA (Bajpai et al., 2017; Brazete et al., 2018). It can be noticed from **Figure 3(d)** that the α/β-TCP phase has completely disappeared in the higher synthesis temperature grown samples, and a pure HA phase is achieved. This indicates the impact of synthesis temperature on the stabilization of the HA phase.

3.3 Vibrational Mode Study of PO_3^{4-} Molecules in β-TCP and HA Phases

To further corroborate the findings of XRD, we have employed the Raman spectroscopy measurements on a few of the samples, and the results are presented in **Figure 4**. The as-synthesized samples (with variable Ca/P ratios and variable synthesis temperature) are presented in **Figure 4(a-c)**. Similarly, the 800°C calcined samples (synthesized at variable Ca/P ratios and variable synthesis temperature) are presented in **Figure 4(d-f)**. It is noticeable from **Figure 4(a-c)** that, despite the variation in the Ca/P ratios and synthesis temperatures, the as-synthesized samples have shown an intense Raman active mode at ~ 963 cm^{-1}. This mode is due to the symmetric stretch of P - O bonds of PO_4^{3-} ligands in CDHA samples (Kim et al., 2015; Montes-Hemandez and Renard, 2020; Filippov et al., 2021; Navarrete-Segado et al., 2022). The appearance of this Raman active mode strengthened the formation of the CDHA phase in all the samples. Interesting variations are seen in the Raman active modes of calcined samples. It is noticeable from **Figure 4(d)** that the *ice-bath* grown sample, followed by calcination at 800°C, has exhibited two distinct Raman active modes at ~ 948 cm^{-1} and 970 cm^{-1}. In previous reports, these two modes have been assigned as the characteristic modes of pure β-TCP (Kim et al., 2015; Montes-Hemandez et al., 2020; Navarrete-Segado et al., 2022). These modes are due to the triply degenerated and stretching modes of P-O bonds. It is visible from **Figure 4(d)** that a distinct band appears at ~ 963 cm^{-1} in the case of 100°C synthesis-temperature grown samples (followed by calcination at 800°C). The appearance of the Raman active mode at ~ 963 cm^{-1} is due to the evolution of the HA phase (Montes-Hemandez et al., 2020; Navarrete-Segado et al., 2022). Moreover, the intensity of the Raman active mode at ~ 963 cm^{-1} is increased for the 200°C synthesis-temperature grown sample (followed by calcination at 800°C). This is in accordance with our XRD findings, where the systematic evolution of the HA phase has been identified. Raman spectra of **Figure 4(e)** show the pronounced intensity of the Raman active mode of HA phase along with the minor peaks of β-TCP phase. The Raman spectra of Ca/P = 1.67 grown samples, **Figure 4(f)**, with variable synthesis temperature, have shown an intense peak of the HA phase and have not shown any reflection of the β-TCP phase. This indicates pure HA formation in this sample and is in accordance with our XRD results.

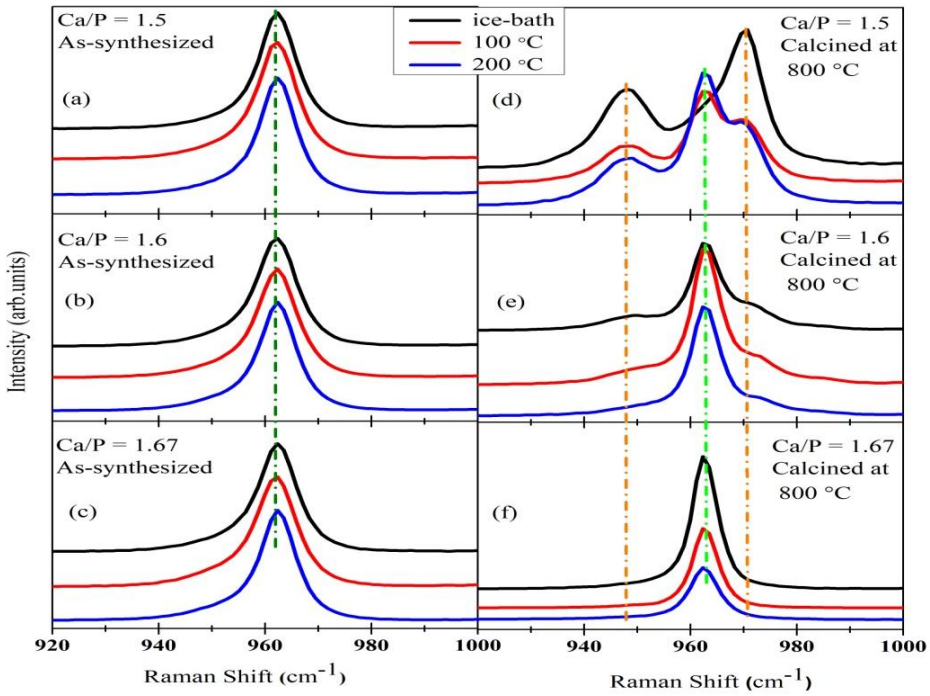

Figure 4. Raman spectra of as prepared CDHA with Ca/P ratio of (a) 1.5, (b) 1.6, (c) 1.67. Raman spectra of calcined samples at 800°C with Ca/P ratio of (d) 1.5, (e) 1.6, (f) 1.67. Each panel has three different spectra collected for different synthesis temperatures conditions namely; ice-bath, 100°C and 200°C.

3.4 Morphology and Elemental Mapping by TEM

To verify the morphology of the as-synthesized and calcined samples, systematic TEM measurements were performed. **Figure 5(a)** and **5(b)** show the TEM images along with elemental mapping of *ice-bath* and 200°C grown samples, respectively, which were synthesized at Ca/P = 1.5. After the calcination at 800°C, TEM images and elemental mapping of these samples were also studied and are presented in **Figure 5(c)** and **5(d)**, respectively. The fast-Fourier transformations (FFT) can give the corresponding diffraction patterns from a high-resolution TEM image (Zhang et al., 2023). Therefore, to examine the crystalline nature of the samples, systematic FFT patterns were generated from the high-resolution images of the crystalline particles and are provided in the inset of the respective TEM images. It is evidenced that the as-synthesized samples (at *ice-bath* and 200°C synthesis conditions) have shown elongated morphology (i.e., nano-rod) and are consistent with many of the previous reports (Liu et al., 2004; Carino et al., 2018; Blum et al., 2021). In the annealed samples, the thermal diffusion of smaller particles to form larger particles has resulted in the morphology transformation (Liu et al., 2004). The elemental mapping of the samples shows that the constituent elements are intimately amalgamated and do not form rich domains of a particular element (see the insets of the elemental analysis image). The quantitative analysis of the elements is provided in **Table 2**. The C and Cu peaks were also detected in the EDS spectra, which were generated from the C-supported Cu grid.

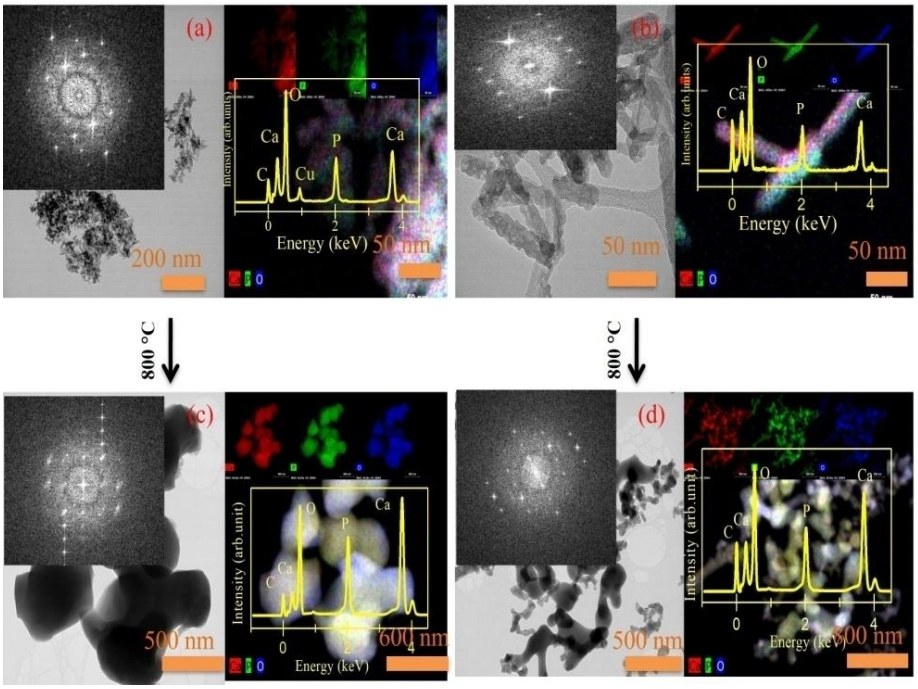

Figure 5. TEM images of; (a) *ice-bath* synthesized CDHA (Ca/P = 1.5), (b) 200°C synthesis temperature prepared CDHA (Ca/P = 1.5), (c) 800°C calcined (grown at *ice-bath* with Ca/P = 1.5) sample, (d) 800°C calcined (grown at 200 °C with Ca/P = 1.5). The elemental mapping, EDS spectrum and FFT patterns from the respective samples are provided in the right and top insets of each image.

Though the nominal Ca/P ratio of the *ice-bath* and 200°C grown samples was the same (i.e., Ca/P = 1.5) but the elemental analysis from **Table 2** conveys a slightly higher Ca/P ratio in the 200°C synthesized sample. This could be due to the participation of larger concentration of Ca^{2+} ions in the higher temperature grown samples. The migration of Ca^{2+} ions to contribute to the CDHA phase formation will be enlightened in the discussion section. The elongated morphology has been transformed into the larger-sized particles of diffused morphology. The brighter fringes in the FFT patterns correspond to the superior crystallinity in the calcined samples and are in accordance with the XRD results. The elemental mapping of the calcined samples indicates the uniform distribution of the elements (see the insets of **Figure 5(c)** and **5(d)**). Besides this, the estimated Ca/P ratio in the calcined samples is nearly the same as that taken, nominally, during the synthesis (see **Table 2**). Since homogeneous distribution of constituent elements and a suitable Ca/P ratio are desired in the artificial bone or dentistry crafts, therefore, our results are of significant promise towards the synthesis of high-quality β-TCP phase formation in the nominal Ca/P = 1.5 samples (synthesized at different synthesis temperature conditions and calcined at 800°C).

Table 2. Ca/P ratios, calculated from the EDS studies, of various samples. The EDS has uncertainty, in analyzing the elemental concentrations, ranging from ±0.1–1wt %.

Nominal Ca/P ratios↓	Calculated Ca/P ratios (in parentheses)	
	as-synthesized samples	Calcined samples at 800 °C
Ca/P = 1.5	*Ice-bath* (1.25)	*Ice-bath* (1.56)
	200 °C (1.40)	200 °C (1.63)
Ca/P = 1.67	*Ice-bath* (1.32)	*Ice-bath* (1.69)
	200 °C (1.60)	200 °C (1.79)

Similar to the samples of nominal Ca/P = 1.5, the samples of nominal Ca/P = 1.67 were also studied by TEM, and the results are presented in **Figure 6(a-d)**. **Figure 6(a)** shows the TEM results of the *ice-bath* synthesized sample, and **Figure 6(b)** shows the TEM results of 200°C synthesis temperature grown sample. It is evidenced by **Figure 6**(**a** and **b**) that the samples are showing a nano-rod kind of morphology and are consistent with the findings of Ca/P = 1.5 grown samples of this study. The bright spots in the FFT patterns exhibit the crystalline nature of the samples. The elemental mapping also exhibits a homogeneous distribution of the constituent elements (see the insets of **Figure 6(a)**, and **(b)**). The nano-rod morphology has vanished after calcination at 800°C and merged/cobbled particles of larger size are grown (see **Figure 6(c)** and **(d)**). The FFT patterns of the calcined samples also exhibit the intense fringes, which correspond to the high crystallinity of the powders and are in accordance with our XRD results. Elemental mapping of the calcined samples also indicates the homogeneous distribution of Ca, P, and O species and strengthening the god-quality ceramic formation. The as-synthesized samples (**Figure 6(a)** and **(b)**) have shown a slightly lower Ca/P ratio than that of the nominal Ca/P ratio (see the **Table 2**). This could be due to the Ca^{2+} ion deficiencies in the as-synthesized CDHA phase and is in accordance with the previous reports (Kannan et al., 2005; Abdel-Fattah et al., 2008; Elgharbawy et al., 2024; Mutlu et al., 2024; Viragova et al., 2024). **Table 2** shows that nearly the same Ca/P ratios as that of the nominal Ca/P ratio are seen in the 800°C calcined samples. This indicates the formation of good-quality hydroxyapatite products in the present study.

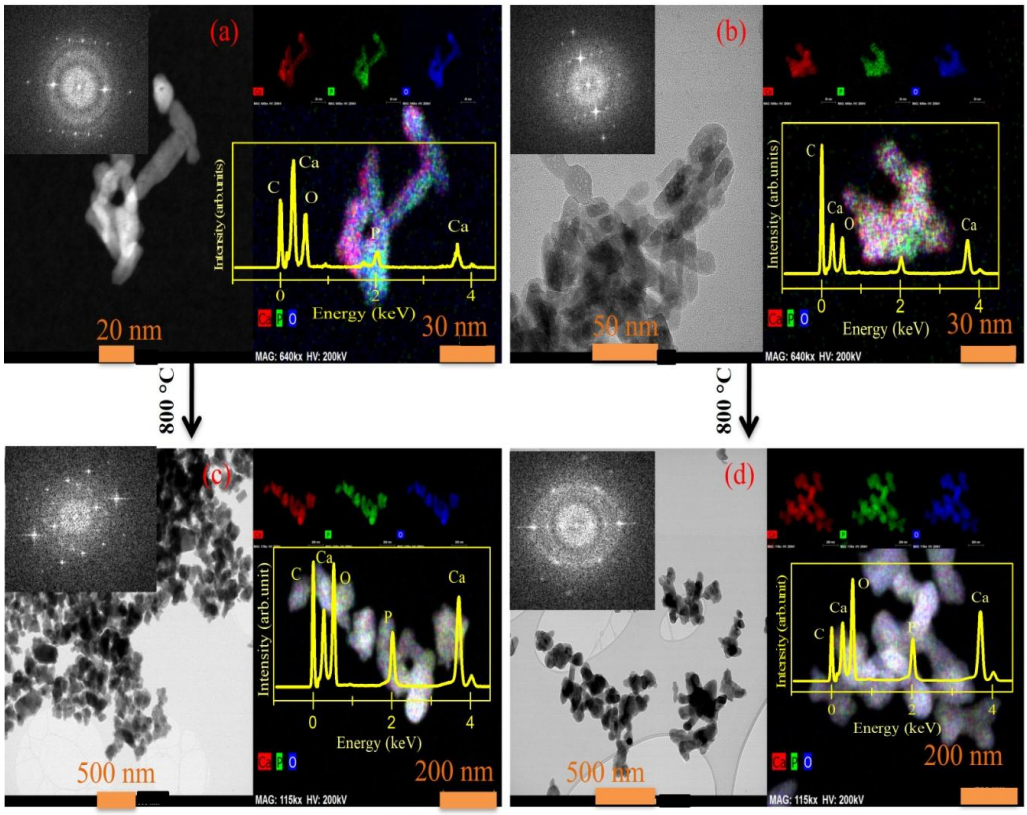

Figure 6. TEM images of; (a) *ice-bath* synthesized CDHA (Ca/P = 1.67), (b) 200°C synthesis temperature prepared CDHA (Ca/P = 1.67), (c) 800°C calcined (grown at *ice-bath* with Ca/P = 1.67) sample, (d) 800°C calcined (grown at 200°C with Ca/P = 1.67). The elemental mapping, EDS spectrum and FFT patterns from the respective samples are provided in the right and top insets of each image.

4. Discussion on the Thermal Energy-Induced Migration of Ca^{2+} Ions and Growth of Phases in the Samples

It is known that the precipitation rates depend on the driving force for the precipitation and are, indeed, regulated by the reaction temperature, ionic activity product, and solubility product (Lima et al., 2020; Balbuena et al., 2021). It has been known that the driving force for the precipitation of a certain phase at a given temperature is the difference in Gibbs free energy between the supersaturated and equilibrium solution and is given as (Lima et al., 2020; Balbuena et al., 2021).

$$\Delta G = -\frac{RT}{n}\ln\frac{X}{k_{sp}} \quad (1)$$

where, the R is universal gas constant, T is the temperature, X is the ionic activity product, n is the number of ions and k_{sp} is the solubility product. From the above relation, it is apparent that the greater driving force for precipitation and, hence, significant precipitation or growth of a certain phase is expected with increasing the temperature or ionic activity product and decreasing the k_{sp}. In the present study, the lower temperature-grown samples (especially the *ice-bath* prepared sample) are expected to have less precipitation and, thus, the growth of smaller-sized crystallites is observed in our XRD studies (see the calculated particle size in **Table 1**). On the other hand, the higher synthesis temperature grown sample is expected to exhibit higher precipitation, and, thus, the growth of larger-sized particles is evidenced in this study.

We further anticipate that higher temperature synthesized samples (for example, 200°C synthesized sample) have not only accomplished the higher precipitation of CDHA phase but the higher ionic activity product is also attained. High ionic activity product indicates lesser Ca^{2+} ions in the solution with increasing the temperature, i.e., many Ca^{2+} ions are expected to contribute to the phase formation rather than roaming in the solution (Lima et al., 2020; Balbuena et al., 2021). On the other hand, the low temperature grown samples may have larger Ca^{2+} ions in the solution, rather participating in the phase formation, because of a lesser driving force for the reaction at a lower temperature. Thus, the lower temperature-grown CDHA may have higher Ca^{2+} ion deficiencies. From the above discussion, we also predict that the higher synthesis temperature-grown CDHA may have a higher proportion of HA phase upon calcination because of appropriate Ca^{2+} ions assimilation.

The molecular-level mechanism of the β-TCP or HA formation can be given in the form of a chemical reaction. It is accepted that the Ca deficiency, indeed, controls the growth of the components of biphasic apatite upon the calcination of CDHA (Mandic et al., 2023).

$$Ca_{10-x}(HPO_4)_x(PO4)_{6-x}\,(OH)_{2-x} \rightarrow (1-x)Ca_{10}(PO_4)_6(OH)_2 + 3xCa_3(PO_4)_2 + xH_2O \quad (2)$$

In the above equation, the formation of bi-phasic (β-TCP + HA) powders is predictable if x is less than 1. Transformation of CDHA into pure β-TCP is possible, provided that the Ca^{2+} deficiency in CDHA is high enough, i.e., $x = 1$.

$$Ca_{10-x}\,(HPO_4)_x(PO_4)_{6-x}\,(OH) \rightarrow 3Ca_3(PO_4)_2 + H_2O \quad (3)$$

In the theoretical studies, it was predicted that the pure β-TCP phase could be grown if the Ca/P ratio is fixed to 1.5 (Basu and Basu, 2019; Dorozkin, 2021). In contrast to that, experimental studies have shown that the pure β-TCP can be achieved at the lower Ca/P ratios provided that the Ca deficiencies are good enough in the as-prepared CDHA (Glazov et al., 2022; Zhang et al., 2022; Humbert et al., 2024). Our XRD results infer that pure β-TCP phase at Ca/P = 1.4 (*ice-bath* and room temperature conditions) can be achieved if the Ca^{2+} deficiencies are enough (i.e., $x = 1$ in Equation (2)). The less Ca^{2+} deficient CDHA

(i.e., $x < 1$) offers binary phase formation upon calcination, according to Equation (1), and is also observed in our XRD results. The Ca^{2+} deficiencies free CDHA, indeed, favor the pure HA phase formation (Saska et al., 2017; Cestari et al., 2021; Zhang et al., 2022). Elimination of β-TCP phase and formation of pure HA can be understood from equation 1, if $x = 0$. Thus, our XRD results of **Figure 3(d)** and Equation (1) are convincing that the Ca/P = 1.67 and synthesis temperature ≥ 50°C are the favorable conditions to achieve the pure HA phase, where the Ca^{2+} ion deficiencies were negligible (i.e., Ca/P ratio was nearly 1.67; see **Table 2**).

5. Conclusions

Fabrication of single-phase calcium phosphate powders (pure CDHA, pure β-TCP, and pure HA) is achieved by the wet-chemical method. A range of synthesis temperatures (*ice-bath* to 200°C) was applied to synthesize the samples with different Ca/P ratios (Ca/P = 1.4, 1.5, 1.6 and 1.67), while the pH of the solution was kept constant (=10) and the calcination temperature was 800°C. XRD and Raman results have confirmed the CDHA phase formation in the as-synthesized samples, despite variations in the nominal Ca/P ratio and synthesis temperatures. However, the degree of crystallinity, average particle size, and calculated Ca/P ratios were subjected to the synthesis temperature. Our experimental results and molecular mechanism of phase formation indicate that the Ca^{2+} ion migration towards the precipitation of CDHA phase is regulated by the Gibbs free energy of the solution, which, indeed, depends on the applied synthesis temperature. Thus, superior crystallinity and higher Ca/P ratios are achieved in the higher synthesis temperature (200°C) grown CDHA, compared with lower temperature (*ice-bath*) grown CDHA. The calcination, at 800°C, of the as-synthesized CDHA phase leads to pure β-TCP, pure HA, and BCP phase formation, depending on the nominal Ca/P ratios and applied synthesis temperatures. The samples prepared with Ca/P ratio = 1.4 and 1.5 (*ice-bath* condition) and calcined at 800 °C have transformed into pure β-TCP phase. On the other hand, a pure HA phase is achieved after the calcination of the samples, which were grown at Ca/P ratio = 1.67 and a synthesis temperature of ≥ 50°C. The rest of the combinations of either Ca/P ratios or synthesis temperature could produce BCP ceramics.

Conflicts of Interest

The authors declare that they have no known competing financial interests or personal relationships that could have appeared to influence the work reported in this paper.

Acknowledgments

Aditya Sharma is thankful to the Uttarakhand State Council for Science and Technology (UCOST, Dehradun) for financial support under the R&D project scheme (UCOST-RND-39/2024-UCOST-DPT/26805). The data used to support the findings of this study are included in the article. Raw data that supports the findings of this study are available from the corresponding author, upon reasonable request.

AI Disclosure

The author(s) declare that no assistance is taken from generative AI to write this article.

References

Abdel-Fattah, W.I., Reicha, F.M., & Elkhooly, T.A. (2008). Nano-beta-tricalcium phosphates synthesis and biodegradation: 1. Effect of microwave and SO42− ions on β-TCP synthesis and its characterization. *Biomedical Materials*, *3*(3), 034121. https://doi.org/10.1088/1748-6041/3/3/034121.

Bajpai, I., Kim, D.Y., Kyong-Jin, J., Song, I.H., & Kim, S. (2017). Response of human bone marrow-derived MSCs on triphasic Ca-P substrate with various HA/TCP ratio. *Journal of Biomedical Materials Research Part B: Applied Biomaterials*, *105*(1), 72-80.

Balbuena, O.B.F., Paiva, L.F.S., Ribeiro, A.A., Monteiro, M.M., de Oliveira, M.V., & Pereira, L.C. (2021). Sintering parameters study of a biphasic calcium phosphate bioceramic synthesized by alcoholic sol-gel technique. *Ceramics International*, *47*(23), 32979-32987.

Basu, S., & Basu, B. (2019). Unravelling doped biphasic calcium phosphate: synthesis to application. *ACS Applied Bio Materials*, *2*(12), 5263-5297.

Blum, M., Sayed, M., Mahmoud, E.M., Killinger, A., Gadow, R., & Naga, S.M. (2021). In vitro evaluation of biologically derived hydroxyapatite coatings manufactured by high velocity suspension spraying. *Journal of Thermal Spray Technology*, *30*(7), 1891-1904.

Brazete, D., Abrantes, J.C.C., & Ferreira, J.M.F. (2018). Influence of the Ca/P ratio and cooling rate on the allotropic α↔ β-tricalcium phosphate phase transformations. *Ceramics International*, *44*(7), 8249-8256.

Bristy, N.S., Kawsar, M., & Hossain, M.S. (2025). Effects of different types of modifiers on structural variation of nano-hydroxyapatite for efficient application. *Nanoscale Advances*, *7*(17), 5133-5160.

Carino, A., Ludwig, C., Cervellino, A., Müller, E., & Testino, A. (2018). Formation and transformation of calcium phosphate phases under biologically relevant conditions: experiments and modelling. *Acta Biomaterialia*, *74*, 478-488.

Cestari, F., Agostinacchio, F., Galotta, A., Chemello, G., Motta, A., & M. Sglavo, V. (2021). Nano-hydroxyapatite derived from biogenic and bioinspired calcium carbonates: synthesis and in vitro bioactivity. *Nanomaterials*, *11*(2), 264. https://doi.org/10.3390/nano11020264.

Chen, D., Mei, D., Chen, L., Wang, C., Bai, J., Xue, F., Chu, C., Wang, L., Zhu, S., & Guan, S. (2024). A ceria/calcium-phosphate functional composite coating on magnesium alloy for enhanced adhesion strength, corrosion resistance, and biocompatibility. *Applied Surface Science*, *672*, 160790. https://doi.org/10.1016/j.apsusc.2024.160790.

Daculsi, G. (1998). Biphasic calcium phosphate concept applied to artificial bone, implant coating and injectable bone substitute. *Biomaterials*, *19*(16), 1473-1478.

Das, A., Ghosh, S., Ringu, T., & Pramanik, N. (2023). A focus on biomaterials based on calcium phosphate nanoparticles: an indispensable tool for emerging biomedical applications. *BioNanoScience*, *13*(2), 795-818.

Dorozhkin, S.V. (2012). Biphasic, triphasic and multiphasic calcium orthophosphates. *Acta Biomaterialia*, *8*(3), 963-977.

Dorozhkin, S.V. (2021). Synthetic amorphous calcium phosphates (ACPs): preparation, structure, properties, and biomedical applications. *Biomaterials Science*, *9*(23), 7748-7798.

Elgharbawy, H., Hassona, A., & Morsy, R. (2024). Synthesis and biophysical characterization of porous bi-phase calcium phosphate/gelatin-PVA scaffold: enhanced antibacterial, osteoconductivity and anticancer activity via silver nanoparticles and methotrexate incorporation. *Journal of Molecular Structure*, *1311*, 138329. https://doi.org/10.1016/j.molstruc.2024.138329.

Filippov, L.O., Filippova, I.V., Kaba, O.B., & Fornasiero, D. (2021). In-situ study of the kinetics of phosphoric acid interaction with calcite and fluorapatite by Raman spectroscopy and flotation. *Minerals Engineering*, *162*, 106729. https://doi.org/10.1016/j.mineng.2020.106729.

Glazov, I.E., Krut'ko, V.K., Musskaya, O.N., & Kulak, A.I. (2022). Calcium phosphate apatites: wet formation, thermal transformations, terminology, and identification. *Russian Journal of Inorganic Chemistry*, *67*(2), 173-182.

He, L., Dong, G., & Deng, C. (2016). Effects of strontium substitution on the phase transformation and crystal structure of calcium phosphate derived by chemical precipitation. *Ceramics International*, *42*(10), 11918-11923.

Hossain, M.S., Shaikh, M.A.A., Uddin, M.N., Bashar, M.S., & Ahmed, S. (2023). β-tricalcium phosphate synthesized in organic medium for controlled release drug delivery application in bio-scaffolds. *RSC Advances*, *13*(38), 26435-26444.

Hu, Y., Wan, L., Xiao, Y., Wang, Y., Wu, Z., Guo, W., Yang, H., & Hu, T. (2022). Enhanced reparative dentinogenesis of biphasic calcium phosphate ceramics containing calcium-deficient hydroxyapatite (CDHA) and strontium-incorporated CDHA in direct pulp capping. *Materials Today Communications*, *33*, 104231. https://doi.org/10.1016/j.mtcomm.2022.104231.

Humbert, P., Kampleitner, C., De Lima, J., Brennan, M.Á., Lodoso-Torrecilla, I., Sadowska, J.M., Blanchard, F., Canal, C., Ginebra, M.P., Hoffmann, O., & Layrolle, P. (2024). Phase composition of calcium phosphate materials affects bone formation by modulating osteoclastogenesis. *Acta Biomaterialia*, *176*, 417-431. https://doi.org/10.1016/j.actbio.2024.01.022.

Kannan, S., Rocha, J.H.G., Ventura, J.M.G., Lemos, A.F., & Ferreira, J.M.F. (2005). Effect of Ca/P ratio of precursors on the formation of different calcium apatitic ceramics—An X-ray diffraction study. *Scripta Materialia*, *53*(11), 1259-1262.

Kim, D.H., Hwang, K.H., Lee, J.D., Park, H.C., & Yoon, S.Y. (2015). Long and short range order structural analysis of in-situ formed biphasic calcium phosphates. *Biomaterials Research*, *19*(1), Article ID: s40824-015-0036-0. https://doi.org/10.1186/s40824-015-0036-0.

Li, X., Deng, Y., Wang, M., Chen, X., Xiao, Y., & Zhang, X. (2018). Stabilization of Ca-deficient hydroxyapatite in biphasic calcium phosphate ceramics by adding alginate to enhance their biological performances. *Journal of Materials Chemistry B*, *6*(1), 84-97.

Lima, D.B., de Souza, M.A.A., de Lima, G.G., Souto, E.P.F., Oliveira, H.M.L., Fook, M.V.L., & de Sá, M.J.C. (2020). Injectable bone substitute based on chitosan with polyethylene glycol polymeric solution and biphasic calcium phosphate microspheres. *Carbohydrate Polymers*, *245*, 116575. https://doi.org/10.1016/j.carbpol.2020.116575.

Liu, J., Li, K., Wang, H., Zhu, M., & Yan, H. (2004). Rapid formation of hydroxyapatite nanostructures by microwave irradiation. *Chemical Physics Letters*, *396*(4-6), 429-432. https://doi.org/10.1016/j.cplett.2004.08.094.

Luo, F., Yang, Y., Li, D., Mao, R., Huang, Y., Lu, J., Zhu, X., Wang, K., Fan, Y., & Zhang, X. (2025). Low-temperature plasma effect-induced enhancement of osteogenic activity in calcium phosphate ceramics. *Acta Biomaterialia*, *200*, 667-685. https://doi.org/10.1016/j.actbio.2025.04.048.

Mandic, V., Radovanovic-Peric, F., Panzic, I., & Vrsaljko, D. (2023). Addressing of different synthetic and shaping approaches for 13-tri calcium phosphate macro-microporous scaffold fabrication. *Ceramics International*, *49*(9), 14934-14940.

Montes-Hernandez, G., & Renard, F. (2020). Nucleation of brushite and hydroxyapatite from amorphous calcium phosphate phases revealed by dynamic in situ Raman spectroscopy. *The Journal of Physical Chemistry C*, *124*(28), 15302-15311.

Mutlu, B., Demirci, F., & Duman, Ş. (2024). Influence of boron incorporated biphasic calcium phosphate on mechanical, thermal, and biological properties of poly (vinylidene fluoride) membrane scaffold. *Journal of the American Ceramic Society*, *107*(11), 7274-7288.

Navarrete-Segado, P., Frances, C., Tourbin, M., Tenailleau, C., Duployer, B., & Grossin, D. (2022). Powder bed selective laser process (sintering/melting) applied to tailored calcium phosphate-based powders. *Additive Manufacturing*, *50*, 102542. https://doi.org/10.1016/j.addma.2021.102542.

Pillai, R.S., & Sglavo, V.M. (2015). Effect of MgO addition on solid state synthesis and thermal behavior of beta-tricalcium phosphate. *Ceramics International*, *41*(2), 2512-2518.

Raudonyte-Svirbutaviciene, E., Lukaviciute, L., Moravec, Z., Pinkas, J., Goto, T., Sekino, T., Zarkov, A., & Kareiva, A. (2023). Tailoring hydroxyapatite morphology via the effect of divalent cations on the hydrolysis of α-TCP: oriented crystal growth towards the application in water treatment. *Ceramics International*, *49*(20), 32816-32825.

Samanta, S.K., Devi, K.B., Das, P., Mukherjee, P., Chanda, A., Roy, M., & Nandi, S.K. (2019). Metallic ion doped tri-calcium phosphate ceramics: effect of dynamic loading on in vivo bone regeneration. *Journal of the Mechanical Behavior of Biomedical Materials*, *96*, 227-235.

Saska, S., Teixeira, L.N., de Castro Raucci, L.M.S., Scarel-Caminaga, R.M., Franchi, L.P., Dos Santos, R.A., Santagneli, S.H., Capela, M.V., de Oliveira, P.T., Takahashi, C.S., Gaspar, A.M.M., Messaddeq, Y., Ribeiro, S.J.L., & Marchetto, R. (2017). Nanocellulose-collagen-apatite composite associated with osteogenic growth peptide for bone regeneration. *International Journal of Biological Macromolecules*, *103*, 467-476. https://doi.org/10.1016/j.ijbiomac.2017.05.086.

Varshney, M., Sharma, A., Shin, H.J., Chae, K.H., Lee, B.H., & Won, S.O. (2025). Effect of nominal Ca/P ratios on the growth of calcium phosphate phases: An in-situ and ex-situ XRD investigation. *Materials Chemistry and Physics*, *348*, 131593. https://doi.org/10.1016/j.matchemphys.2025.131593.

Vilela, H.S., Rodrigues, M.C., Fronza, B.M., Trinca, R.B., Vichi, F.M., & Braga, R.R. (2021). Effect of temperature and pH on calcium phosphate precipitation. *Crystal Research and Technology*, *56*(12), 2100094.

Viragova, E.S., Novotna, L., Chlup, Z., Stastny, P., Sarfy, P., Cihlar, J., Kucirek, M., Benak, L., Streit, L., Kocanda, J., Sklensky, J., Filipovic, M., Repko, M., Hampl, A., Koutná, I., & Castkova, K. (2024). Porous silica-doped calcium phosphate scaffolds prepared via in-situ foaming method. *Ceramics International*, *50*(21), 41215-41227.

Yang, A., Huang, H., Li, J., Yang, L., Li, S., Chang, D., Bai, Z., Duan, G., Guo, T., & Weng, J. (2023). Regulating the multifactor during wet chemical synthesis to obtain calcium phosphate powders with controllable phase purity for bone repair. *Ceramics International*, *49*(15), 25302-25311.

Zhang, L., Lu, T., He, F., Zhang, W., Yuan, X., Wang, X., & Ye, J. (2022). Physicochemical and cytological properties of poorly crystalline calcium-deficient hydroxyapatite with different Ca/P ratios. *Ceramics International*, *48*(17), 24765-24776.

Zhang, Q., Bai, R., Peng, B., Wang, Z., & Liu, Y. (2023). FFT pattern recognition of crystal HRTEM image with deep learning. *Micron*, *166*, 103402.